Chemistry—Methods

Research Article
doi.org/10.1002/cmtd.202400069

Chemistry Europe
European Chemical Societies Publishing

www.chemistrymethods.org

Monitoring Nanostructural Dynamics During the Electrochemical Growth of Metal Hydroxide Thin Films by *in-situ* Small-Angle X-Ray Scattering

Jonas Schwan,[a] Sabine Rosenfeldt,[b, c] and Anna S. Schenk*[a, c]

Understanding structural dynamics on the nanoscale is essential for progress in current research areas such as catalysis, energy storage, and nanotechnology. In this study, we introduce an in-house electrochemical flow cell for real-time small-angle X-ray scattering (SAXS) experiments to monitor cobalt hydroxide ($Co(OH)_2$) electrocrystallization under controlled conditions. $Co(OH)_2$ films were produced *via* cathodic electrochemical deposition (CED) from a $Co(NO_3)_2$ solution. SAXS data, complemented by electron microscopy and spectroscopy, reveal the formation of nanoscale $Co(OH)_2$ platelets with an average thickness of ~13 nm and a lateral size of ~600 nm. Time-resolved *in-situ* SAXS tracks the steady growth of these platelets, from 7.8 nm to 15.7 nm thickness over 120 min. In addition, SAXS measurements demonstrate the influence of citrate ligands, which initially suppress platelet formation and stabilize spherical nanostructures. As citrate depletes in the electrolyte, platelets begin to form, indicating a dynamic shift in crystallization mechanism. By employing *in-situ* SAXS, we successfully monitor the temporal evolution of nanoscale structures, offering insights into the mechanisms governing crystallization under electrochemically controlled conditions. These findings underscore the versatility of in-house SAXS setups for real-time analysis of material formation and growth processes, with implications for tailoring the synthetic parameters towards materials with dedicated nanostructures for various technological applications.

Introduction

The study of structural dynamics is crucial for understanding a wide range of material systems, particularly at the nanoscale, as it provides insights into the fundamental processes that govern material behavior, stability, and performance. By observing how atomic and nanoscale structures evolve over time – whether during phase transitions, chemical reactions, or under mechanical stresses – researchers can better predict and control material properties such as strength, conductivity, and reactivity. This knowledge is particularly valuable in fields like catalysis, energy storage, and nanotechnology, where precise control over nanostructure formation, reorganization and transformation directly impacts the efficiency and functionality of devices.[1–4] Moreover, understanding these dynamics aids the identification of optimal conditions for material synthesis and processing, thus enabling the design of more resilient, efficient, and sustainable materials for advanced technological applications.

Notably, pioneering work by Herron *et al.* in 1992 showcased the ability of *in-situ* X-ray diffraction (XRD) to monitor structural changes in electrochemically controlled redox systems, such as oxidizing platinum electrodes.[5] In the early 2000s, J. R. Dahn's group expanded this research to study the insertion and extraction of alkali metals, such as lithium and sodium, in the crystal lattices of layered metal oxides and silicon, thus making valuable contributions toward an in-depth understanding of battery materials.[6–9] Recent publications by various groups have addressed similar questions about the dynamics of crystallographic structures in electrode materials under electrochemical conditions.[10–13] Most of this research utilized in-house *in-situ* XRD setups, which allowed for precise control over simple experimental variables, including electrochemical parameters, e.g. current and potential, and low temperatures, as shown in the monitoring of low-temperature formation in reactive multilayer systems.[14] However, studies requiring high-pressure conditions or fast-time resolution were typically conducted at synchrotron beamlines.[15–17] Williamson *et al.* were the first to introduce liquid cell transmission electron microscopy (TEM) to monitor the growth of solid phases from liquid solutions using imaging techniques, allowing for direct nanoscale observation of electrochemical copper deposition in real time.[18] Since its inception, *in-situ* TEM has been extensively utilized to study the growth and degradation of nanocrystals across a wide range of material systems and morphologies.[19–23] In combination with the electrochemical deposition technique, *in-situ* TEM was also employed for the analysis of magnesium

[a] *Physical Chemistry IV, Department of Chemistry, University of Bayreuth, Bayreuth, Germany*
[b] *Physical Chemistry I, Department of Chemistry, University of Bayreuth, Bayreuth, Germany*
[c] *Bavarian Polymer Institute, University of Bayreuth, Bayreuth, Germany*
***Correspondence:** Prof. Anna S. Schenk, Physical Chemistry IV, Department of Chemistry, University of Bayreuth, Universitaetsstrasse 30, 95447 Bayreuth, Germany.*
Email: anna.schenk@uni-bayreuth.de

Supporting Information for this article is available on the WWW under https://doi.org/10.1002/cmtd.202400069

crystallization providing insights into current issues and the chemistry of Mg ion batteries.[24] Additionally, liquid cell TEM has proven highly effective for *in-situ* tracking of shape transformations induced by corrosion or etching[25,26], as well as for capturing metastable phases during dynamic processes.[27]

While methods such as liquid cell TEM and *in-situ* electrochemical XRD have provided complementary insights into nanoscale and lattice scale processes, *in-situ* SAXS holds unique advantages to examine a size range of 1–300 nm. Liquid cell TEM allows for real-time imaging of nanostructures in liquids but is often limited in terms of probing bulk sample volumes or monitoring long-duration experiments. Further limits, especially for high-resolution TEM, include the difficulties caused by radiolysis of water and the reductive environment.[28] Most importantly, TEM as a semi-quantitative method is less suitable to extract structure parameters with high statistical accuracy. *In-situ* electrochemical XRD, on the other hand, excels in crystallographic analysis but lacks the ability to resolve amorphous or less-ordered nanostructures. Synchrotron-based *in-situ* SAXS setups can be used complementarily to fill in the gaps left by the aforementioned methods. Extensive research has been conducted on polymer crystallization and structural changes in polymer systems in response to external stimuli.[29–35] Additionally, *in-situ* SAXS at synchrotron facilities has increasingly been employed to analyze the nucleation and growth of metallic nanoparticles.[36–39] These experiments also enable the proof of hierarchical structures formed from nanoscale building blocks.[40–42] *In-situ* SAXS is further applied in monitoring the fabrication of thin metallic films through sputter deposition.[43–48] In electrochemical environments, *in-situ* SAXS can, for instance, be used for time-resolved tracking of the electrochemical crystallization of metallic nanoparticles or metal oxides, as well as the degradation of catalyst materials.[49–55] In many cases, *in-situ* SAXS is coupled with other measurement techniques, most commonly X-ray diffraction (XRD) or wide-angle X-ray scattering (WAXS). However, coupling with dynamic light scattering (DLS)[37], ultraviolet-visible (UV-Vis) spectroscopy[39], or X-ray absorption spectroscopy (XAS)[38] is also possible. In some instances, even three techniques are combined, such as *in-situ* SAXS, WAXS, and quick-scanning extended X-ray absorption fine structure (QEXAFS)[56], or *in-situ* SAXS, WAXS, and atomic force microscopy (AFM)[57]. These examples highlight the vast range of applications and the significant utility of synchrotron-based *in-situ* SAXS setups.

However, such setups come with inherent limitations – access to synchrotron facilities is scarce, experimental flexibility is constrained, and extended monitoring over long durations can be logistically challenging. In contrast, recent advances in in-house SAXS setups offer a flexible and convenient alternative as they provide a wide range of material compatibility, the possibility of monitoring processes over extended periods of time, and the flexibility to conveniently adjust reaction parameters. A combination of *in-situ* SAXS, WAXS and UV-Vis was used at an in-house device by Chen *et al.* (2015) to study the nucleation and growth of gold nanoparticles.[58] Tillier *et al.* (2016) pioneered the development of a custom-built *in-situ* SAXS cell suitable for conventional, non-synchrotron-based X-ray sources.[59] This innovation demonstrated the potential for more accessible and adaptable SAXS experiments. Their studies, which explored Ostwald ripening during oxygen reduction reactions (ORR) on platinum-based catalysts, emphasized the value of in-house SAXS systems for long-term monitoring of nanoscale processes. Another example for diffraction experiments using a laboratory instrument is the work of Pickering *et al.* which monitors the crystallization of magnesium chlorides by simultaneous SAXS/WAXS experiments.[60]

In this study, we introduce a novel in-house flow cell for electrochemical deposition experiments designed for real-time, time-resolved SAXS measurements. This system provides a highly adaptable sample environment capable of monitoring nanostructure evolution, as demonstrated in the electrocrystallization of nanostructured cobalt hydroxide ($Co(OH)_2$), which is an important precursor for cobalt oxides that have application as catalysts in the electrolysis of water. As a well-studied model system, spinel-type cobalt(II,III) oxide (Co_3O4) can be used as an electrocatalyst for both oxidation and reduction of water into oxygen and hydrogen, respectively. It is also highly active in a broad pH range. However, low efficiency and high overpotentials still prevent large-scale industrial applications with the oxygen evolution reaction (OER) being the bottleneck in the development of the process.[61] One promising idea for improving catalytic properties of electroactive materials is nano-structuring, as this approach increases the reactive surface area.[62,63] In the past, our group successfully gained control over the nanostructure of cobalt oxide precursors which could be preserved during conversion into the catalytically active Co_3O_4 phase.[64–68] However, it remains an intriguing question to monitor the nanostructural dynamics of such materials to gain a more detailed understanding, and make progress towards controlling and tuning nanostructures of electroactive materials. Furthermore, our setup enables facile, long-term analysis, while omitting the limitations associated with synchrotron-based systems, thus paving the way for future in-house studies across a broader range of material systems and experimental conditions.

Experimental Details

Chemicals and Materials

Cobalt nitrate hexahydrate ($Co(NO_3)_2{\cdot}6H_2O$) and sodium citrate ($Na_3C_6H_5O_7$) were purchased in analytical grade from Merck KGaA (Darmstadt, Germany). Hellmanex III solution was purchased from Hellma GmbH & Co. KG (Müllheim, Germany). All chemicals were applied directly as received from the suppliers without further purification and aqueous solutions were prepared with deionized water (resistivity 18.2 MΩ cm, Milli-Q Advantage A10, Merck).

Copper tape (3 M Scotch 1181, thickness of copper film: 66 μm) was purchased from 3 M (Saint Paul, MN, USA). The tape stripes used as electrodes were cleaned in an ultrasonic bath for 10 min, sequentially immersed in aqueous Hellmanex III solution (5 wt%), acetone, ethanol, and aqueous NaOH solution

(1 mol L^{-1}) within glass vials. After each step, the substrates were rinsed with the corresponding solvent and air-dried at room temperature.

Construction of the Electrochemical Flow Cell and Sample Preparation

The custom-built electrochemical flow cell (EFC) is made of polyether ether ketone and was fabricated by the mechanical workshop of the University of Bayreuth according to CAD sketches. The EFC consists of three main components, which are vertically aligned, and two electrically conductive copper foils which suit as electrodes. Central recesses in each component form windows that allow the X-ray beam to pass through for small-angle X-ray scattering (SAXS) measurements. In preparation for the deposition experiments, the aqueous electrolyte solutions containing $Co(NO_3)_2$ (10 mmol L^{-1}) and additionally sodium citrate (2 mmol L^{-1}) for the citrate-directed crystallization experiments were injected into the reaction chamber which is formed by the recess in the middle part of the cell and the two copper foils. The latter were then connected to a potentiostat through special perforations adjacent to the reaction chamber using gold screws.

Eletrochemical Deposition of $Co(OH)_2$ Thin Films

Ex-situ electrochemical depositions within the electrochemical flow cell were performed and monitored by using a *PGSTAT204* potentiostat (Metrohm Autolab B.V., Utrecht, Netherlands). Copper tape was used as working electrode and counter electrode, respectively, in a two-electrode setup. During *in-situ* SAXS experiments the electrochemical parameters were set with an Aim TTi *PLH250* potentiostat (TTI, Inc., Fort Worth, TX, USA). For electrochemical formation of the $Co(OH)_2$ thin films, a constant current density of -0.25 mA cm^{-2} was applied for 120 min. After the deposition the films were rinsed with water and dried at ambient conditions.

Structural and Compositional Characterization

The structure and composition of electrochemically deposited cobalt hydroxide precipitates prepared in the absence and presence of structure-directing citrate were analyzed using a combination of imaging, scattering and spectroscopy methods.

General morphologies and detailed structures of the samples were imaged by scanning electron microscopy (SEM) using a Zeiss LEO 1530 VP Gemini from Carl Zeiss AG (Oberkochen, Germany) operated at an acceleration voltage of 3 kV. In preparation for SEM measurements, the substrates supporting the inherently conductive electrodeposited specimens were mounted on a standard sample holder. Sputter coating of the samples was not necessary because the films themselves are electrically conductive. Colloidal silver (Ted Pella, Inc., Redding, CA, USA) was used to establish an electrical contact between the sample holder and the cobalt hydroxide film.

SAXS experiments were performed using a Double Ganesha AIR system from SAXSLAB/Xenocs. Monochromatic radiation (λ = 1.54 Å) was provided by a rotating anode (generator: MicroMax-007HF) from Rigaku Corporation (Tokyo, Japan). Two-dimensional scattering patterns were collected with a position-sensitive PILATUS 300 K detector from Dectris (Philadelphia, PA, USA) which was placed at different distances from the sample. The radially averaged profiles of the scattering intensity *I(q)* versus the modulus of the scattering vector *q*, which is given as $q = |\vec{q}| = 4\pi/\lambda \cdot \sin(\theta/2)$ with λ representing the wavelength of the incident beam and θ the scattering angle, were corrected for background (in our case the $Co(NO_3)_2$ solution in the cell prior to electrodeposition of solids), an assumed sample thickness of 3 mm (similar to the distance between the two copper foils in the electrochemical flow cell), accumulation time as well as absorption, and subsequently merged using the SAXSutilities software (version 4.99).[69] Data fitting was conducted with the SasView software (version 5.0.6).[70]

Raman spectroscopy was performed with a LABRAM I Raman Spectrometer (HORIBA Jobin Yvon SAS, Edison, NJ, United States of America). The instrument was equipped with a BX41 microscope (Olympus Corporation, Tokyo, Japan), and a He-Ne-Laser (λ = 632.82 nm) with a laser power of 1.15 mW was applied as a radiation source. Spectra were acquired in a wavenumber range between 50 cm^{-1} and 1000 cm^{-1}, with a 50x magnification objective measuring an average of 20 scans à 2 s exposition time. LabSpec 5.78.24 software was used for data evaluation. The electrodeposited samples were analyzed directly on the electrode substrates with the Raman spectrometer without further treatment.

Fourier-Transform Infrared (FT-IR) spectroscopy was performed with a *Tensor 27* FT-IR spectrometer equipped with a mid-IR source, a KBr beamsplitter, and a DGST detector (Bruker, Billerica, MA, United States of America). The measurements were carried out in a wavenumber range of 4000 cm^{-1} to 600 cm^{-1} and spectra were processed and evaluated with *Opus* software.

Results and Discussion

Introducing an Electrochemical Flow Cell for In-House SAXS Monitoring of Electrodeposition Processes

The electrochemical flow cell (EFC) configuration for *in situ* electrocrystallization assessments was adapted from the design previously reported by Tillier *et al.*.[59] As illustrated in Figure 1, the EFC comprises three primary components denoted as I, II, and III, respectively, which were custom-fabricated from polyether ether ketone, based on CAD-sketches. These parts are vertically aligned and fastened using metallic screws through four designated apertures as depicted in Figure 1a. Central recesses are incorporated into each component to form windows allowing for unimpeded passage of the X-ray beam for SAXS measurements.

Research Article
doi.org/10.1002/cmtd.202400069
Chemistry Europe
European Chemical Societies Publishing

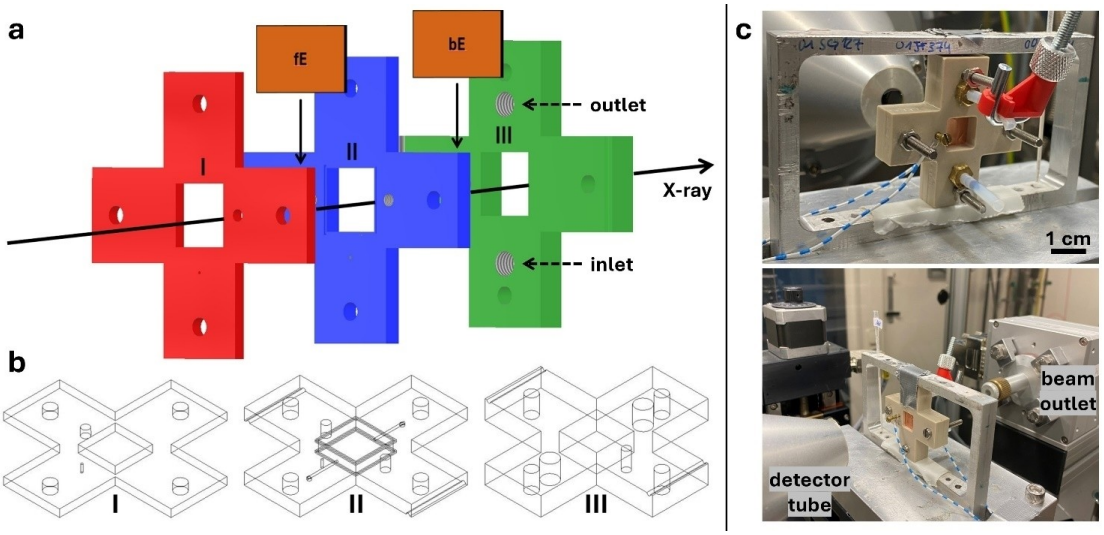

Figure 1. (a) Electrochemical flow cell (EFC) components (I, II, and III) aligned with two conductive foils (fE and bE) to form an electrolyte-filled cell compartment while enabling the passage of an X-ray beam through the window. For better visibility, the components are represented in different colors. (b) Schematic drawings of the electrochemical flow cell parts, particularly highlighting the inner channels in component II. (c) Photographs of the assembled EFC installed in the sample chamber of the SAXS instrument.

Specifically, conductive copper foils, are interposed between components I and II, and II and III, respectively, serving as electrodes. The electrodes within the EFC are designated as the front electrode (fE), positioned between components I and II, and the back electrode (bE), situated between components II and III. The foils serve as anode or cathode, respectively, during electrochemical experiments, thus configuring the setup into a two-electrode system. The final stacking order, proceeding from the top downward, is as follows: I – fE – II – bE – III. Each foil is connected to the electrical setup *via* gold screws, with those for the front electrode inserted through holes passing through components III and II before contacting fE, and those for the back electrode inserted through holes passing through components I and II before reaching bE. Consequently, the front electrode is accessed from the rear of the cell (with respect to the direction of the X-ray beam), while the back electrode is accessed from the front. Additionally, part III features two holes, serving as inlets for introducing reagent solutions. Female pneumatic contacts are installed into III to accommodate the attachment of polytetrafluoroethylene (PTFE) tubing. These holes in III, marked by dashed arrows in Figure 1a, connect to channels within part II, as depicted in Figure 1b. The inlets enable the injection of reagent solutions filling both the channels within II and the electrolyte chamber enclosed by the two conductive foils. The reaction chamber has a volume of 0.3 mL (1 cm x 1 cm x 0.3 cm). Part II is equipped with two O-rings for effective sealing. The modularity of the EFC, composed of three distinct parts, ensures ease of assembly and disassembly, facilitating electrode exchange and chamber cleaning between different experiments. Photographs of the assembled EFC, installed in the SAXS instrument used for this work, are shown in Figure 1c. A metallic frame holder is used for effective sample alignment perpendicular to the X-ray beam.

Nanostructural Dynamics of the Electrochemically Induced $Co(OH)_2$ Thin Film Growth

Cobalt hydroxide films were produced by cathodic electrochemical deposition (CED) under galvanostatic conditions using the flow cell for SAXS analysis. The design of the cell determines the exposed surface area of the copper tape, which is used for both electrodes, to be 1 cm^2 and fixes the distance between the electrodes at 3 mm. An aqueous solution of $Co(NO_3)_2$ (10 mmol L^{-1}) was used as electrolyte. To induce galvanostatic deposition at the cathode, a constant current of 0.25 mA cm^{-2} was applied. A thin film of $Co(OH)_2$ with a substructure of nanoscale platelets is obtained by electrodeposition for 60 minutes as observed by scanning electron microscopy (SEM) analysis (Figures 2a). Additional SEM images with various magnification are provided in Figure S1 in the supporting information (SI) and show a homogenous distribution of upright standing $Co(OH)_2$ platelets over the entire surface of the copper foil. Raman and infrared (IR) spectroscopy confirm that the deposited film is composed of α-$Co(OH)_2$ (Figure S2) based on comparison of the spectroscopic signature with literature data.[71–73] The potential response during the galvanostatic CED is displayed in Figure 2b. Initially, the potential drops to ca. – 1.1 V and after the brief stabilization period it increases to a value of – 1.0 V. This increase suggests that an initial coverage with a $Co(OH)_2$ film is built, which then lowers the energy barrier toward the formation of new crystals. After ca. 20 min of deposition (t_{dep}) another decrease in potential can be detected which is presumably due to the decrease in the cobalt ion concentration. Figure 2b also shows a schematic illustration of the redox reaction. Reduction of nitrate anions lead to the formation of hydroxide anions near the cathode according to Equation 1 followed by the precipitation of $Co(OH)_2$ as a homogenous film on the cathode (Equation 2).[74] Additionally,

Research Article
doi.org/10.1002/cmtd.202400069
Chemistry Europe
European Chemical Societies Publishing

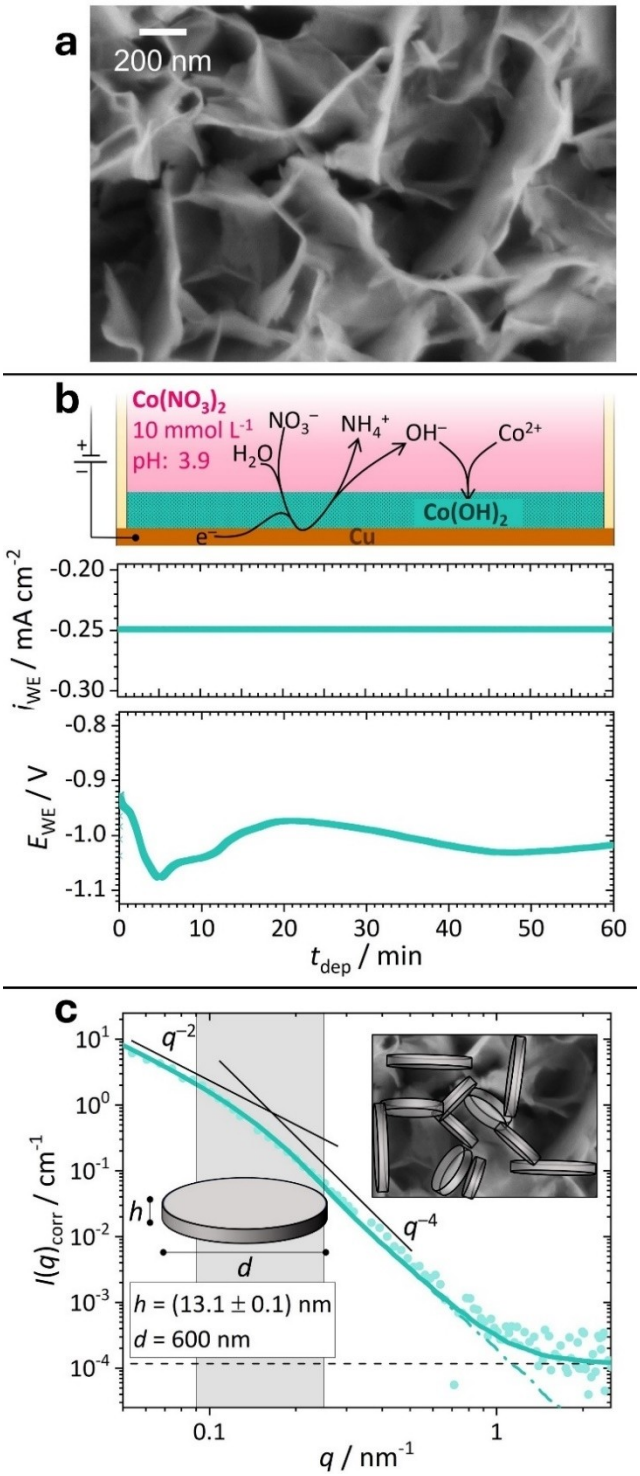

Figure 2. (a) Scanning electron micrograph of the as-deposited $Co(OH)_2$ on copper foil. (b) Schematic illustration (top) of the reaction taking place within the flow cell. Electrochemical monitoring of galvanostatic $Co(OH)_2$ particle growth showing the current density j_{WE} (middle) and the potential E_{WE} (bottom) at the copper foil used as working electrode. (c) Corrected small-angle X-ray scattering intensities $I_{corr}(q)$ *vs.* scattering vector q in a double-logarithmic plot for the deposited $Co(OH)_2$ film (filled circles). A disk model (inset) was fitted to the scattering data revealing the presence of platelets with a thickness of $h = (13.1 \pm 0.1)$ nm.

water reduction can potentially take place, but is very unlikely to occur under the given conditions because the nitrate reduction is favorable and the nitrate concentration sufficiently high.

$$NO_3^- + 7\ H_2O + 8\ e^- \rightarrow NH_4^+ + 10\ OH^- \quad (1)$$

$$Co^{2+} + 2\ OH^- \rightarrow Co(OH)_2 \quad (2)$$

The thickness h of the mature $Co(OH)_2$ platelets was analyzed by an *ex-situ* SAXS measurement of the electrodeposited material as seen in Figure 2c. The scattering profile shows a q^{-2} power law dependence in the region of $q < 0.1\ nm^{-1}$ which develops into a behavior following Porod's law with a characterstic q^{-4} slope for $q > 0.15\ nm^{-1}$. The scattering pattern indicates the presence of a two-dimensional structure which conforms with the SEM images of the sample.

From semi-quantitative, manual SEM image analysis (measurement of 50 single platelets using *Image J*) the dimensions of the platelets can be determined to an average thickness of $h \approx 15$ nm and an average lateral diameter of $d \approx 600$ nm. In the *ex-situ* SAXS measurement a characteristic q^0 power law behavior which would be required to determine the lateral platelet dimension was not obtained in the limited experimental q-range, revealing that the lateral size already exceeded $d = 250$ nm (approximation: $d_{max} = 2\pi/q_{min}$) after electrodeposition which is in agreement with the SEM analysis. The transition area ($0.09\ nm^{-1} \leq q \leq 0.25\ nm^{-1}$) between the q^{-2} and the q^{-4} regions, however, allows for the SAXS-based determination of the platelet thickness h. For this purpose, a cylinder model[75,76] was used because a 2D-disk can be described as a circular cylinder with thickness h and diameter d, where $d \gg h$. While the real structure of the deposits involves the curvature of the platelets and their interconnections, and is challenging to capture even by more complex models, we deliberately chose the cylinder model as a simple representation to describe the disks as we are here mainly interested in their thickness.

Thus, we set the diameter to $d = 600$ nm (based on SEM analysis) and only fitted the disk thickness h. The data also show a constant background (represented as black dashed line in Figure 2c) which causes a deviation from the Porod slope for $q > 0.6\ nm^{-1}$. A cylinder fit with a fitted constant background is shown in Figure 2c (teal curve) along with a cylinder fit performed without a constant background (dotted teal curve). Both curves largely superimpose for $q < 0.6\ nm^{-1}$, which fully covers the q-range where we can extract information about the platelet thickness h. For SAXS analysis we therefore used cylinder fits with $I(q)_{background} = 0$. The differences in thickness between individual platelets are described in the evaluation by a fitted polydispersity index (PDI), which is based on a Gaussian distribution of the platelet thickness. The *ex-situ* SAXS measurement results in an average platelet thickness of $h = (13.1 \pm 0.1)$ nm with a PDI of (0.60 ± 0.01). Please note, that the indicated errors represent fit errors and not absolute errors. Both, the SAXS and the SEM analysis, show comparable results which proofs SAXS to be a suitable method to quantitatively analyze the thickness of nanoscale $Co(OH)_2$ platelets formed by electro-

Research Article
doi.org/10.1002/cmtd.202400069
Chemistry Europe
European Chemical Societies Publishing

chemical deposition. Additionally, SAXS measurements were conducted with a μ-focused beam in different spots/domains on the $Co(OH)_2$ film confirming that the platelet structure is homogeneous throughout the full lateral extension of the film (cf. Figure S3).

The successful analysis of mature films by SAXS, raises the intriguing question whether it is possible to monitor the process of nanoscale platelet growth and potential nanostructural dynamics using scattering methods. Our approach utilizes the presented flow cell for conducting *in-situ* SAXS measurements to draw mechanistic insights into the growth process under variation of the deposition conditions. For this purpose, the crystallization progress was divided into timeframes of 15 min and the scattered radiation was recorded and accumulated for each stage of the reaction. The resulting scattering curves were corrected for sample-related transmission and the contribution of the sample holder, including environmental air background. A measurement of the flow cell right before the CED, hence equipped with copper foils and filled with $Co(NO_3)_2$ solution but not yet featuring a $Co(OH)_2$ film, was used as background signal and subtracted from the data recorded during electrodeposition. For statistical reasons, the experiment was repeated several times to obtain a total of five data sets which were then averaged. The individual data sets for each of the *in-situ* experiments are presented in Figure S4 and the average scattering profiles for each deposition time are provided in Figure S5 in the SI, respectively. All individual scattering curves of each set followed the same trend as the averaged profile, but with an inherently lower signal to noise ratio. To monitor the development of $Co(OH)_2$ platelet morphology we extended the overall deposition time to 2 h for the *in-situ* experiments. The above-introduced disc model was applied for the description of all *in-situ* data in a *q*-range of $0.09\ nm^{-1} \leq q \leq 0.25\ nm^{-1}$. Again, the diameter of the disks was set to $d = 600$ nm and the disk thickness *h* was fitted monitoring the time-dependent trend. Our evaluation assumes that the diameter of the platelets *d* already exceeds a value of approximately 140 nm after 15 min of deposition, and is therefore outside the fit range. The choice of $d = 600$ nm therefore has no effect on the result of the *h* determination. Figure 3a shows the scattering profiles obtained during *in-situ* $Co(OH)_2$ growth in a *q*-range of $0.085\ nm^{-1} \leq q \leq 0.55\ nm^{-1}$, and Figure 3b plots the platelet thickness *h*, extracted from the cylinder model fits, as a function of deposition time. In the first hour of the experiment (Figure 3a, left), an increasing overall intensity can be observed and, in addition, a steeper gradient with a longer deposition time. This indicates a development towards larger platelets, whose characteristic Porod decay region shifts into the fit range. The thickness *h* determined from the cylinder fit initially evolves gradually from 7.8 nm after 15 min to 13.0 nm after 60 min and then increases slightly further to a value of 15.7 nm after 120 min of electrodeposition (see Figure 3b). A gradually decreasing growth rate is seen throughout the experiment. The exact results of the evaluation are summarized in Table S1 and the individual scattering profiles are shown in Figure S5, respectively. Since the slope of the SAXS curves does not change further after 60 min, the

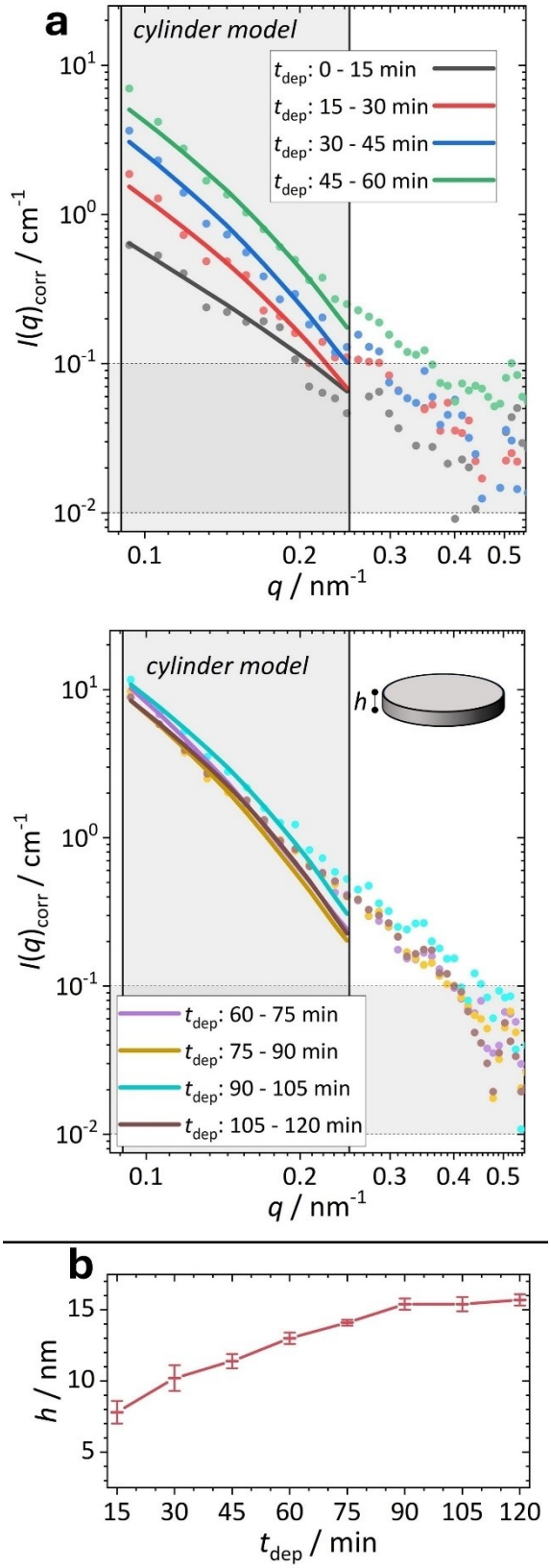

Figure 3. (a) Corrected small-angle X-ray scattering intensities $I_{corr}(q)$ *vs.* scattering vector *q* in a double-logarithmic plot for different stages of the electrochemical growth of the additive-free $Co(OH)_2$ film conducted in the flow cell for *in-situ* SAXS measurements. (b) Plot of the platelet thickness as a function of deposition time based on the fitting results for each timeframe.

Research Article
doi.org/10.1002/cmtd.202400069
Chemistry Europe
European Chemical Societies Publishing

higher intensity of the curves in the second half of the experiment can also be explained by an increased number of fully grown mature platelets. In addition, the scattering profiles obtained for the early timeframes are overall noisier, which means that the values for h are less confident for short deposition times. However, the experiment shows that we initially see an increase in the platelet thickness h, which tends towards a plateau with no further increase over time. The result for h from the *in-situ* experiment after $t_{dep} = 60$ min strongly agrees with that from the *ex-situ* measurement (cf. Figure 2c).

Electrochemical Growth of $Co(OH)_2$ Films under the Influence of Citrate as a Structure-Directing Additive

As discussed above, the here-presented flow cell endows us with the possibility to monitor the electrochemical growth of $Co(OH)_2$ platelets *via in-situ* SAXS experiments. To test our setup for compatibility with other nanoscale morphologies, and to expand the range of mechanistic test cases, we extended the experiment and investigated the influence of sodium citrate on the (nano−)morphology of cobalt hydroxide films, which were produced by CED under galvanostatic conditions with the same parameters as the additive-free control sample. An aqueous solution of $Co(NO_3)_2$ (10 mmol L^{-1}) and $Na_3C_6H_5O_7$ (2 mmol L^{-1}) was used as electrolyte. To induce galvanostatic deposition at the cathode, a constant current of −0.25 mA cm^{-2} was applied. Again, the local formation of hydroxide anions at the cathode leads to precipitation of $Co(OH)_2$ as shown in Figure 4b. In the presence of citrate, however, no homogenous thin film is obtained, but inspection of SEM micrographs and semiquantitative analysis using the *Image J* software rather point to an accumulation of larger spherical aggregates with radius $R =$ 500 nm, consisting of individual spherical subunits of $r = 57$ nm (Figure 4a). Additional SEM images of the as-deposited citrate-mediated $Co(OH)_2$ films are presented in Figure S6 in the SI. A comparison with literature-reported Raman and IR spectroscopy data reveals that, chemically, the films can be assigned to the α-$Co(OH)_2$ phase with citrate being present in the solid deposits, as seen in Figure S7 in the SI.[71–73,77] The mature deposits were then analyzed by an *ex-situ* SAXS measurement, cf. Figure 4c. The SAXS profile exhibits a scaling behavior with $I(q)$ proportional to $q^{-2.6}$ for $q < 0.08$ nm^{-1}, which transitions to a $q^{-3.7}$ power law behavior in the regime of larger q with $q >$ 0.08 nm^{-1}. This slope remains constant until the profile transitions into a flat background for $q > 0.6$ nm^{-1}. As the SEM analysis revealed fractal-like aggregates, the experimental data are then compared to the theoretical scattering curve of a mass-surface-fractal consisting of smaller spherical subunits.[78,79] SEM analysis reveals that the aggregates exhibit an overall radius of approximately R = 500 nm, i.e. the scattering signals of these motifs fall outside the detectable q range, as the radius exceeds 125 nm. The subunits, however, exhibited an accessible radius of r = 57 nm. These parameters were kept constant during the evaluation using the mass-surface-fractal model, and the mass fractal dimension D_m and surface fractal dimension D_s were fitted. The best agreement with the experimental data

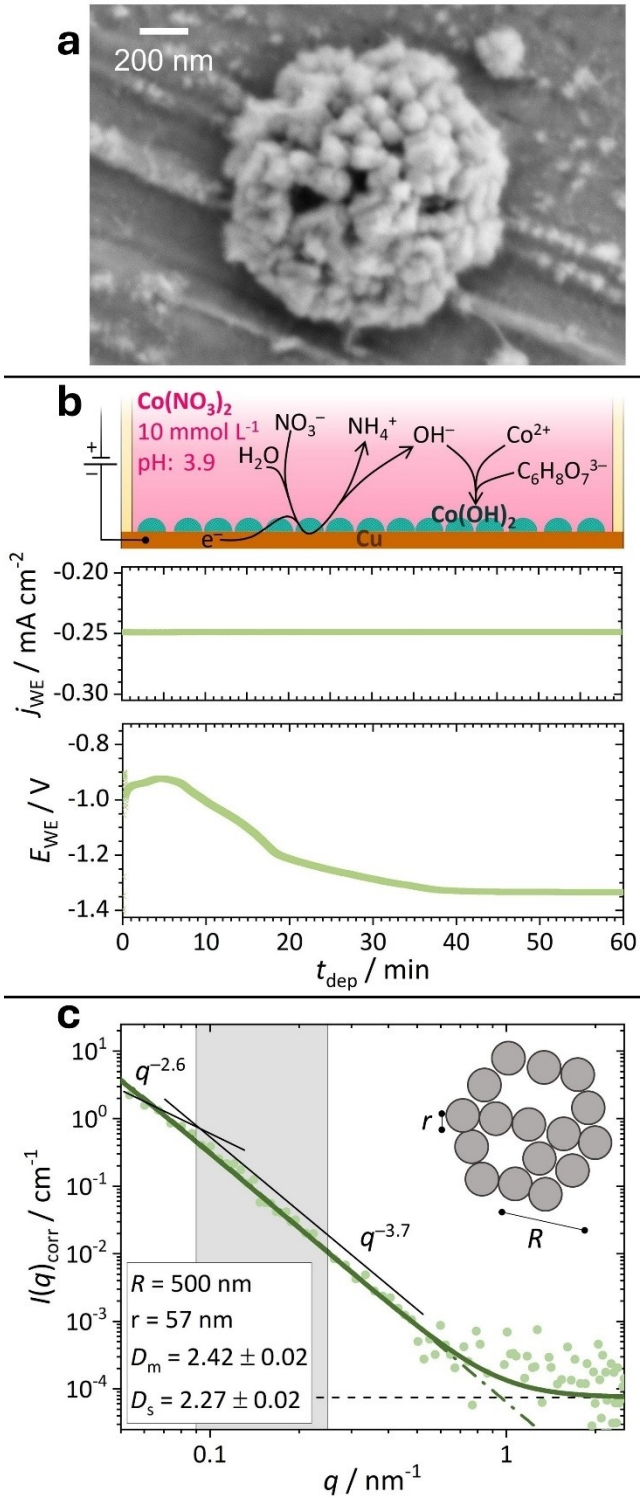

Figure 4. (a) Scanning electron micrograph of the as-deposited $Co(OH)_2$ particles on copper foil revealing spherical aggregates. (b) Schematic illustration (top) of the reaction taking place within the flow cell. Electrochemical monitoring of galvanostatic $Co(OH)_2$ particle growth under the influence of citrate showing the current density j_{WE} (middle) and the potential E_{WE} (bottom) at the copper foil used as working electrode. (c) Corrected small-angle X-ray scattering intensity $I_{corr}(q)$ *vs.* scattering vector q in a double-logarithmic plot for the deposited $Co(OH)_2$ particles. A mass-surface-fractal model for spherical aggregates with radius $R = 500$ nm consisting of subunits with radius $r = 57$ nm (inset) was fitted to the raw data.

Research Article
doi.org/10.1002/cmtd.202400069
Chemistry Europe
European Chemical Societies Publishing

was obtained for specific values of $D_m = 2.42 \pm 0.02$ and $D_s = 2.27 \pm 0.02$. A surface fractal dimension of $D_s = 2$ would correspond to smooth surfaces, which is ruled out based on the SEM images of the particles. The influence of surface fractals is visible in the q-range of $0.09\ nm^{-1} \leq q \leq 0.25\ nm^{-1}$, where the SAXS profile follows a $q^{-3.7}$ behavior. In this regime, $I(q)$ is roughly proportional to $q^{-(6-D_s)}$, which is typical for surface fractals.[80] From the slope in this region, we can infer the surface fractal dimension of the small particles. Figure 4c again shows a constant background (black dashed line) for $q > 0.6\ nm^{-1}$. The SAXS data can be described by a mass-surface-fractal model based on the discussed parameters either with a constant background (green curve) or with $I(q)_{background} = 0$ (dotted green curve).

In-situ experiments using the flow cell were once again performed to monitor the structural dynamics during the citrate-mediated growth of $Co(OH)_2$ particles. These experiments, as previously described, employed time intervals of 15 min, and each experiment was repeated five times. The individual datasets for each *in-situ* experiment, as well as the averaged scattering curves, are shown in the SI in Figures S8 and S9, respectively. Figure 5 presents the time-resolved SAXS measurement of $Co(OH)_2$ deposition under the influence of citrate for $0.085\ nm^{-1} < q < 0.55\ nm^{-1}$. For analysis, the slope of each SAXS profile was determined in the q-range of $0.09\ nm^{-1} < q < 0.25\ nm^{-1}$. Initially, an increase in the absolute value of the exponent was observed: while the first dataset followed a $q^{-3.25}$ power law, the slope changed to a $q^{-3.71}$ behavior between 45 min and 60 min of deposition. Importantly, the latter value matches the result of *ex-situ* experiment (Figure 4c), confirming the presence of a mass-surface fractal with $D_s = 2.3$. The gradual formation of aggregates, as seen in Figure 4a, becomes evident in these *in-situ* measurements. However, it is also noticeable that for deposition times longer than 60 minutes, the curves deviate from the $q^{-3.7}$ slope for $q > 0.17\ nm^{-1}$, shifting towards a less steep decay, particularly visible in the bottom graph of Figure 5, corresponding to longer deposition times. The SAXS profiles of the four later time frames exhibit a different q-dependency, approximately following a $q^{-2.6}$ power law. We can explain the change in slope for long deposition times with several hypotheses: First, it is possible that an increased deposition of $Co(OH)_2$ particles creates more interfaces, which manifests as a shift in the scattering profile in the mid-q range.

Another explanation could be the formation of smaller particles, whose Porod region would appear at higher q-values, leading to a flattening of the overall scattering curve in the examined range. The most probable cause, however, is the overgrowth of the aggregates by an unaffected platelet-like $Co(OH)_2$ film. Chemically, this can be attributed to the decreasing citrate concentration during deposition, by which the influence of the additive on crystallization diminishes over time. This results in the formation of platelet-like structures, as previously shown in Figure 2a. Additionally, after 120 min of deposition, the sample was analyzed *ex-situ* using SEM and SAXS. The SEM micrographs confirmed the visible overgrowth of the particles with platelets, and the SAXS profile followed a

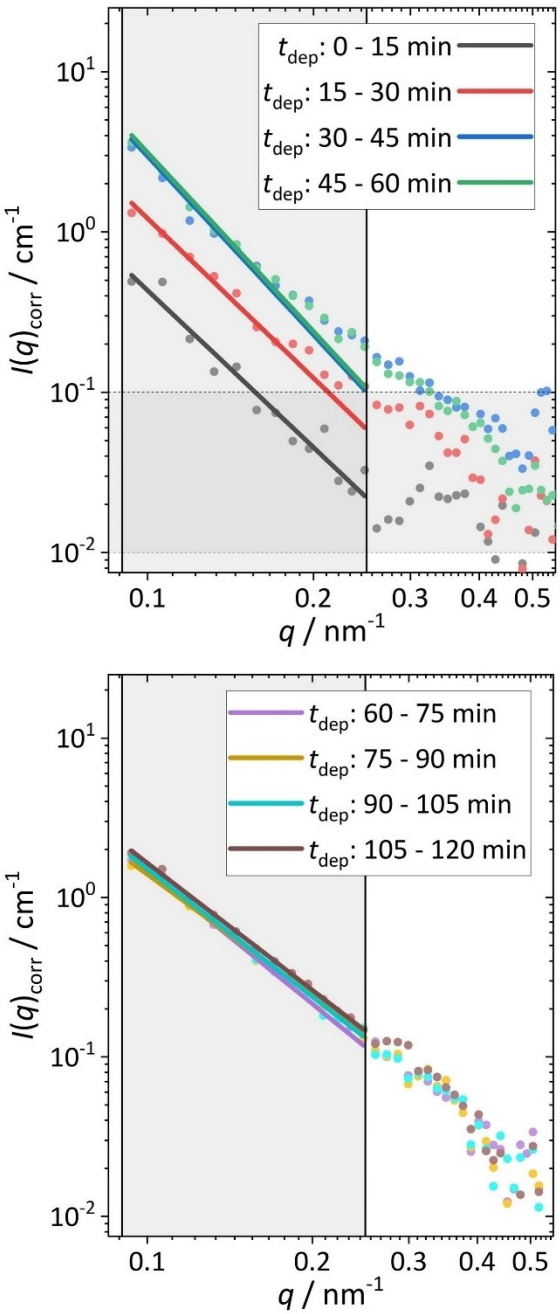

Figure 5. Corrected small-angle X-ray scattering intensities $I_{corr}(q)$ *vs.* scattering vector q in a double-logarithmic plot for different stages of the electrochemical growth of the $Co(OH)_2$ film under the influence of citrate anions conducted in the flow cell for *in-situ* SAXS measurements.

similar trend as the *in-situ* measurements, showing a $q^{-2.6}$ slope for $q > 0.15\ nm^{-1}$ (cf. Figure S10). While a detailed elucidation of the crystallization mechanism remains an intriguing question, it is beyond the scope of this study, which focuses on the introduction and application of the developed flow cell. Nevertheless, this experiment demonstrates how *in-situ* SAXS measurements can provide deep insights into crystallization mechanisms during electrodeposition. For the model system examined in this chapter, these findings provide initial clues regarding such mechanisms. A potential crystallization mecha-

nism involves the nucleation of spherical $Co(OH)_2$ nanostructures, where citrate ligands act as stabilizing agents. These ligands suppress the growth of plate-like crystals but are insufficient to fully inhibit particle aggregation, resulting in the formation of spherical aggregates composed of densely packed nanoscale subunits. As the citrate concentration decreases below a critical threshold, the crystallization of $Co(OH)_2$ nanoplatelets proceeds similar to the additive-free control sample, as presented in the previous chapter.

Conclusions

In this study, we successfully demonstrated the versatility and effectiveness of a custom-built electrochemical flow cell setup for real-time monitoring of the electrocrystallization of $Co(OH)_2$ under various experimental conditions. In a first step, we validated the EFC design through the cathodic electrochemical deposition of additive-free $Co(OH)_2$, confirming the presence of nanoscale platelets using complementary SEM and SAXS techniques. *Ex-situ* SAXS measurements revealed an average platelet thickness of approximately 13 nm, corroborating SEM observations and establishing SAXS as a reliable method for quantitatively analyzing size and shape parameters of the electrodeposited nanostructural motifs. Time-resolved SAXS measurements revealed a gradual increase in platelet thickness over the deposition period, initially rising from 7.8 nm to 15.7 nm over 120 min of deposition, thus indicating that the growth dynamics of this process can be effectively with the tracked *in-situ setup*. The alignment of experimental data with existing literature supports the credibility of our findings and emphasizes the robustness of our methodology.

Subsequently, we explored the effects of sodium citrate as a structure-directing additive on the growth dynamics and morphology of $Co(OH)_2$ films. The presence of citrate induced the formation of larger spherical aggregates rather than a uniform thin film as observed in the control sample, a significant deviation that highlights the role of additives in nanostructure formation. SAXS profiles indicated a mass-surface-fractal behavior demonstrating the influence of citrate on crystallization dynamics. The initial surface fractal dimension of $D_s = 2.27$ suggests a complex interplay between particle aggregation and growth. The *in-situ* SAXS experiments revealed the gradual formation of aggregates, and suggested that as the citrate concentration decreases, crystallization mechanisms shift towards the deposition of plate-like $Co(OH)_2$ structures.

Moreover, this experimental approach opens perspectives for further investigations into the mechanistic understanding of electrocrystallization processes, particularly in view of how different additives affect growth kinetics and final morphologies. As demonstrated by the successful application in the present study, the adaptable flow cell setup provides a valuable platform for future studies aimed at optimizing the synthesis of nanostructured materials, as tailoring of structural motifs is critical for applications in catalysis, energy storage, and environmental remediation.

Overall, our findings underscore the potential of *in-situ* SAXS within the EFC framework for advancing our understanding of nanoscale structural dynamics. This work lays the foundation for future research focused on unraveling the complex mechanisms governing crystallization during electrochemical processes, highlighting the importance of tailoring synthesis conditions to achieve desired nanostructure properties. Future studies could build on this framework by systematically varying the material systems and the concentration of additives, exploring different deposition currents, and employing complementary characterization techniques to provide a more comprehensive understanding of the underlying mechanisms.

Acknowledgments

This research was funded by the University of Bayreuth as well as the German Research Foundation (DFG), Project No. 492723217 (CRC 1585), subproject A03. Further support was received by the German Academic Scholarship Foundation *via* an individual fellowship to J.S.. We thank the Bavarian Polymer Institute (BPI) for providing access to electron microscopy facilities within the KeyLab "Electron and Optical Microscopy" and to the SAXS infrastructure within the KeyLab "Mesoscale Characterization: Scattering Techniques". We also thank the mechanical workshop of the University of Bayreuth for fabricating the electrochemical flow cell. J.S. thanks the Elite Study Program Macromolecular Science within the Elite Network of Bavaria for support. This work benefited from the use of the SasView application, originally developed under NSF award DMR-0520547. SasView contains code developed with funding from the European Union's Horizon 2020 research and innovation program under the SINE2020 project, grant agreement No 654000. Open Access funding enabled and organized by Projekt DEAL.

Conflict of Interests

The authors declare no conflict of interest.

Data Availability Statement

The research data underpinning this article are available from the corresponding author upon request.

Keywords: cobalt hydroxide · electrodeposition · nanostructure · thin films · X-ray scattering

[1] H. Mistry, A. S. Varela, S. Kühl, P. Strasser, B. R. Cuenya, *Nat. Rev. Mater.* **2016**, *1*.
[2] A. L. M. Reddy, S. R. Gowda, M. M. Shaijumon, P. M. Ajayan, *Adv. Mater.* **2012**, *24*, 5045.
[3] F. Zaera, *Chem. Soc. Rev.* **2013**, *42*, 2746.

[4] Y. Zhang, Q. Zhou, J. Zhu, Q. Yan, S. X. Dou, W. Sun, *Adv. Funct. Mater.* **2017**, *27*, 1702317.
[5] M. E. Herron, S. E. Doyle, S. Pizzini, K. J. Roberts, J. Robinson, G. Hards, F. C. Walsh, *J. Electroanal. Chem.* **1992**, *324*, 243.
[6] J. M. Paulsen, C. L. Thomas, J. R. Dahn, *J. Electrochem. Soc.* **2000**, *147*, 861.
[7] Z. Lu, J. R. Dahn, *J. Electrochem. Soc.* **2001**, *148*, A1225.
[8] T. D. Hatchard, J. R. Dahn, *J. Electrochem. Soc.* **2004**, *151*, A838.
[9] J. Li, J. R. Dahn, *J. Electrochem. Soc.* **2007**, *154*, A156.
[10] K. J. Rhodes, R. Meisner, M. Kirkham, N. Dudney, C. Daniel, *J. Electrochem. Soc.* **2012**, *159*, A294.
[11] M. Galceran, D. Saurel, B. Acebedo, V. V. Roddatis, E. Martin, T. Rojo, M. Casas-Cabanas, *Phys. Chem. Chem. Phys.* **2014**, *16*, 8837.
[12] H. Hau, T. Mishra, C. Ophus, T. Huang, K. Bustilo, Y. Sun, X. Yang, T. Holstun, X. Zhao, S. Wang, Y. Ha, G. Lee, C. Song, J. Turner, J. Bai, L. Ma, K. Chen, F. Wang, W. Yang, B. D. McCloskey, Z. Cai, G. Ceder, *Nat. Nanotechnol.* **2024**, 10.1038/s41565-024-01787-y.
[13] Y. Xu, R. Quan, J. Zhou, H. Mao, C. Li, S. Ma, J. Mou, H. Zhou, *Sep. Purif. Technol.* **2025**, *355*, 129761.
[14] M. O. Nnajim, D. A. Tavakoli, D. A. Hitchcock, E. M. Vogel, *J. Appl. Phys.* **2024**, *136*, 115302.
[15] C. S. de Matos, M. M. Nóbrega, M. L. A. Temperini, V. R. L. Constantino, *Appl. Clay Sci.* **2019**, *174*, 152.
[16] T. Komabayashi, C. McGuire, S. Thompson, G. D. Bromiley, A. Bravenec, A. Pakhomova, *J. Geophys. Res. [Solid Earth]* **2024**, *129*, e2024JB029641.
[17] K. K. Pandey, V. I. Levitas, C. Park, G. Shen, *J. Appl. Phys.* **2024**, *136*, 115901.
[18] M. J. Williamson, R. M. Tromp, P. M. Vereecken, R. Hull, F. M. Ross, *Nat. Mater.* **2003**, *2*, 532.
[19] M. H. Nielsen, D. Li, H. Zhang, S. Aloni, C. Frandsen, J. Seto, J. F. Banfield, H. Cölfen, J. James, M. H. Nielsen, D. Li, H. Zhang, S. Aloni, T. Y. Han, C. Frandsen, J. Seto, J. F. Ban, H. Cölfen, J. J. De Yoreo, *Microsc. Microanal.* **2014**, *20*, 425.
[20] G. Zhu, S. Prabhudev, J. Yang, C. M. Gabardo, G. A. Botton, L. Soleymani, *J. Phys. Chem. C* **2014**, *118*, 22111.
[21] J. P. Patterson, P. Abellan, M. S. Denny, C. Park, N. D. Browning, S. M. Cohen, J. E. Evans, N. C. Gianneschi, *J. Am. Chem. Soc.* **2015**, *137*, 7322.
[22] J. Tian, D. Lin, X. Li, K. Wang, B. Yu, M. Li, S. Hou, Z. Li, Q. Chen, *Small* **2024**, 2400680.
[23] S. Lee, T. Watanabe, F. M. Ross, J. H. Park, *Small* **2024**, 2403969.
[24] Y. A. Wu, Z. Yin, M. Farmand, Y. S. Yu, D. A. Shapiro, H. G. Liao, W. I. Liang, Y. H. Chu, H. Zheng, *Sci. Rep.* **2017**, *7*, 42527.
[25] S. W. Chee, S. H. Pratt, K. Hattar, D. Duquette, F. M. Ross, R. Hull, *Chem. Commun.* **2015**, *51*, 168.
[26] F. Liu, H. Tan, Z. Bian, G. Zheng, P. Gao, *Microsc. Microanal.* **2024**, *30*, 1709.
[27] J. Hong, J. Bae, H. Jo, H. Park, S. Lee, S. J. Hong, H. Chun, M. K. Cho, J. Kim, J. Kim, Y. Son, H. Jin, J. Suh, S. Kim, H. Roh, K. H. Lee, H. Kim, K. Y. Chung, C. W. Yoon, K. Lee, S. H. Kim, J.-P. Ahn, H. Baik, G. H. Kim, B. Han, S. Jin, T. Hyeon, J. Park, C. Y. Son, Y. Yang, Y.-S. Lee, S. J. Yoo, D. W. Chun, *Nature* **2022**, *603*, 631.
[28] S. Pu, C. Gong, A. W. Robertson, *R. Soc. Open Sci.* **2020**, *7*, 10.1098/rsos.191204.
[29] G. Kumaraswamy, R. K. Verma, J. A. Kornfield, F. Yeh, B. S. Hsiao, *Macromolecules* **2004**, *37*, 9005.
[30] S. Humbert, O. Lame, J. M. Chenal, C. Rochas, G. Vigier, *Macromolecules* **2010**, *43*, 7212.
[31] S. Humbert, O. Lame, J.-M. Chenal, C. Rochas, G. Vigier, *J. Polym. Sci. Part B Polym. Phys.* **2010**, *48*, 1535.
[32] C. Lei, R. Xu, Z. Tian, H. Huang, J. Xie, X. Zhu, *Macromolecules* **2018**, *51*, 3433.
[33] H. Guo, R. G. Rinaldi, S. Tayakout, M. Broudin, O. Lame, *Mech. Mater.* **2024**, *198*, 105137.
[34] S. Nakagawa, *Phot. Fact. Act. Rep.* **2024**, *41*.
[35] H. An, J. Guo, J. Gao, Y. Zhong, Y. Li, Z. Wang, *J. Polym. Sci.* **2024**, *62*, 3947.
[36] W. Wang, X. Chen, Q. Cai, G. Mo, L. S. Jiang, K. Zhang, Z. J. Chen, Z. H. Wu, W. Pan, *Eur. Phys. J. B* **2008**, *65*, 57.
[37] D. J. Tobler, S. Shaw, L. G. Benning, *Geochim. Cosmochim. Acta* **2009**, *73*, 5377.
[38] J. Polte, T. T. Ahner, F. Delissen, S. Sokolov, F. Emmerling, A. F. Thünemann, R. Kraehnert, *J. Am. Chem. Soc.* **2010**, 1296.
[39] X. Chen, J. Wang, R. Pan, S. Roth, S. Förster, *J. Phys. Chem. C* **2021**, *125*, 1087.
[40] Z. Wu, H. Liu, M. Zhao, X. Wang, W. Cheng, Z. Wu, X. Xing, *Mater. Today Commun.* **2023**, *37*, 107458.
[41] Y. Xi, X. Deng, Z. Shu, C. Yang, *J. Mech. Behav. Biomed. Mater.* **2024**, *156*, 106599.
[42] F. Pignon, E. Guilbert, S. Mandin, N. Hengl, M. Karrouch, B. Jean, J. Putaux, T. Gibaud, S. Manneville, T. Narayanan, *J. Colloid Interface Sci.* **2024**, *659*, 914.
[43] G. Kaune, M. A. Ruderer, E. Metwalli, W. Wang, S. Couet, K. Schlage, R. Röhlsberger, S. V. Roth, P. Müller-Buschbaum, *ACS Appl. Mater. Interfaces* **2009**, *1*, 353.
[44] M. Schwartzkopf, A. Buffet, V. Körstgens, E. Metwalli, K. Schlage, G. Benecke, J. Perlich, M. Rawolle, A. Rothkirch, B. Heidmann, G. Herzog, P. Müller-Buschbaum, R. Röhlsberger, R. Gehrke, N. Stribeck, S. V. Roth, *Nanoscale* **2013**, *5*, 5053.
[45] M. Schwartzkopf, G. Santoro, C. J. Brett, A. Rothkirch, O. Polonskyi, A. Hinz, E. Metwalli, Y. Yao, T. Strunskus, F. Faupel, P. Müller-Buschbaum, S. V. Roth, *ACS Appl. Mater. Interfaces* **2015**, *7*, 13547.
[46] M. Schwartzkopf, A. Hinz, O. Polonskyi, T. Strunskus, F. C. Löhrer, V. Körstgens, P. Müller-Buschbaum, F. Faupel, S. V. Roth, *ACS Appl. Mater. Interfaces* **2017**, *9*, 5629.
[47] M. Al-Hussein, M. Schindler, M. A. Ruderer, J. Perlich, M. Schwartzkopf, G. Herzog, B. Heidmann, A. Buffet, S. V. Roth, P. Müller-Buschbaum, *Langmuir* **2013**, *29*, 2490.
[48] L. Song, W. Wang, V. Körstgens, D. Moseguí González, F. C. Löhrer, C. J. Schaffer, J. Schlipf, K. Peters, T. Bein, D. Fattakhova-Rohlfing, S. V. Roth, P. Müller-Buschbaum, *Nano Energy* **2017**, *40*, 317.
[49] J. Ustarroz, J. A. Hammons, Y. Van Ingelgem, M. Tzedaki, A. Hubin, H. Terryn, *Electrochem. Commun.* **2011**, *13*, 1320.
[50] M. Ruge, F. Golks, J. Zegenhagen, O. M. Magnussen, J. Stettner, *Phys. Rev. Lett.* **2014**, *112*, 1.
[51] T. Binninger, E. Fabbri, A. Patru, M. Garganourakis, J. Han, D. F. Abbott, O. Sereda, R. Kötz, A. Menzel, M. Nachtegaal, T. J. Schmidt, *J. Electrochem. Soc.* **2016**, *163*, H906.
[52] S. J. Richardson, M. R. Burton, X. Luo, P. A. Staniec, I. S. Nandhakumar, N. J. Terrill, J. M. Elliott, A. M. Squires, *Nanoscale* **2017**, *9*, 10227.
[53] M. F. Dupont, A. J. Gibson, A. Elbourne, M. Forghani, D. Cross, S. W. Donne, *J. Electrochem. Soc.* **2020**, *167*, 040520.
[54] T. K. Zakharchenko, A. V. Sergeev, A. D. Bashkirov, P. Neklyudova, A. Cervellino, D. M. Itkis, L. V. Yashina, *Nanoscale* **2020**, *12*, 4591.
[55] F. Lv, X. Wang, Y. Liu, H. Jia, S. Li, X. Zhang, X. Xing, Z. Wu, Z. Wu, W. Cheng, *Russ. J. Electrochem.* **2023**, *59*, 1206.
[56] S. Nikitenko, A. M. Beale, A. M. J. van der Eerden, S. D. M. Jacques, O. Leynaud, M. G. O'Brien, D. Detollenaere, R. Kaptein, B. M. Weckhuysen, W. Bras, *J. Synchrotron Radiat.* **2008**, *15*, 632.
[57] S. Zanchi, R. Cipriani, F. D. Dos Santos, S. Tencé-Girault, S. Roland, *Polymer* **2024**, *307*, 127307.
[58] X. Chen, J. Schröder, S. Hauschild, S. Rosenfeldt, M. Dulle, S. Förster, *Langmuir* **2015**, *31*, 11678.
[59] J. Tillier, T. Binninger, M. Garganourakis, A. Patru, E. Fabbri, T. J. Schmidt, O. Sereda, *J. Electrochem. Soc.* **2016**, *163*, H913.
[60] K. S. Pickering, S. Huband, K. L. Shafran, R. I. Walton, *Chemistry-Methods* **2022**, *2*, 10.1002/cmtd.202200033.
[61] F. T. Haase, A. Bergmann, T. E. Jones, J. Timoshenko, A. Herzog, H. S. Jeon, C. Rettenmaier, B. R. Cuenya, *Nat. Energy* **2022**, *7*, 765.
[62] D. Pletcher, *J. Appl. Electrochem.* **1984**, *14*, 403.
[63] M. S. Faber, S. Jin, *Energy Environ. Sci.* **2014**, *7*, 3519.
[64] A. S. Schenk, S. Eiben, M. Goll, L. Reith, E. John, A. N. Kulak, F. C. Meldrum, C. Wege, S. Ludwigs, *Acta Crystallogr. Sect. A* **2016**, *A72*, 55.
[65] A. S. Schenk, S. Eiben, M. Goll, L. Reith, A. N. Kulak, F. C. Meldrum, H. Jeske, C. Wege, S. Ludwigs, *Nanoscale* **2017**, *9*, 6334.
[66] A. S. Schenk, M. Goll, L. Reith, M. Roussel, B. Blaschkowski, S. Rosenfeldt, X. Yin, W. W. Schmahl, S. Ludwigs, *Cryst. Growth Des.* **2020**, *20*, 6407.
[67] V. Gruen, N. Helfricht, S. Rosenfeldt, A. S. Schenk, *Chem. Commun.* **2021**, *57*, 7244.
[68] J. Schwan, S. Rosenfeldt, A. S. Schenk, *Crystals* **2022**, *12*, 1072.
[69] M. Sztucki, T. Narayanan, *J. Appl. Crystallogr.* **2007**, *40*, 459.
[70] The SasView Project, "SasView," can be found under http://www.sasview.org/, **2024**.
[71] U. M. Patil, R. V. Ghorpade, M. S. Nam, A. C. Nalawade, S. Lee, H. Han, S. C. Jun, *Sci. Rep.* **2016**, *6*, 1.
[72] S. Kalasina, P. Pattanasattayavong, M. Suksomboon, N. Phattharasupakun, J. Wutthiprom, M. Sawangphruk, *Chem. Commun.* **2017**, *53*, 709.
[73] R. Li, Z. Hu, X. Shao, P. Cheng, S. Li, W. Yu, W. Lin, D. Yuan, *Sci. Rep.* **2015**, *6*, 1.

Research Article
doi.org/10.1002/cmtd.202400069

[74] A. D. Jagadale, V. S. Jamadade, S. N. Pusawale, C. D. Lokhande, *Electrochim. Acta* **2012**, *78*, 92.
[75] The SasView Project, "Cylinder Model Function," can be found under https://www.sasview.org/docs/user/qtgui/Perspectives/Fitting/models/shape-cylinder.html, **2022**.
[76] J. S. Pedersen, *Adv. Colloid Interface Sci.* **1997**, *70*, 171.
[77] N. Shahbazi, R. Zare-Dorabei, *ACS Omega* **2019**, *4*, 17519.
[78] The SasView Project, "Mass-Surface-Fractal Model," can be found under https://www.sasview.org/docs/user/models/mass_surface_fractal.html, **2018**.
[79] P. W. Schmidt, *J. Appl. Crystallogr.* **1991**, *24*, 414.
[80] H. D. Bale, P. W. Schmidt, *Phys. Rev. Lett.* **1984**, *53*, 596.

Manuscript received: November 18, 2024
Version of record online: March 21, 2025